ORIGINAL ARTICLE

Effective perpendicular boundary conditions in phase-field models using Dirichlet boundary conditions

Soobin Kwak[1] · Seokjun Ham[1] · Jian Wang[2] · Hyundong Kim[3,4] · Junseok Kim[1]

Abstract

The primary objective of this study is to present the temporal and spatial evolution dynamics of two- and three-dimensional phase-field models with Dirichlet boundary conditions on arbitrary shaped domains. We consider the Allen–Cahn (AC), Cahn–Hilliard (CH), nonlocal Cahn–Hilliard (nCH) equations among the phase-field models in this study. The AC equation has been used to model various phenomena, such as motion by mean curvature flows. It can be derived from the Ginzburg–Landau free-energy functional. The CH equation has been applied to many conservative physical phenomena, such as phase separation dynamics. As for the nCH equation, a fourth-order nonlocal nonlinear PDE, it models the microphase separation of diblock copolymers. For these phase-field models, there are various boundary conditions available, such as Neumann, periodic, Dirichlet boundary conditions. In this study, we investigate the phase transformation dynamics of the phase-field models using different Dirichlet boundary conditions. Furthermore, complex-shaped domains can be handled straightforwardly, and a perpendicular boundary condition can be effectively imposed by applying the zero Dirichlet boundary condition. This approach proves to be highly useful and efficient in imposing the perpendicular boundary conditions for complex-shaped domains.

✉ Junseok Kim
cfdkim@korea.ac.kr

Soobin Kwak
soobin23@korea.ac.kr

Seokjun Ham
seokjun@korea.ac.kr

Jian Wang
003328@nuist.edu.cn

Hyundong Kim
hdkim@gwnu.ac.kr

1 Department of Mathematics, Korea University, Seoul 02841, Republic of Korea

2 School of Mathematics and Statistics, Nanjing University of Information Science and Technology, Nanjing 210044, China

3 Department of Mathematics and Physics, Gangneung-Wonju National University, Gangneung 25457, Republic of Korea

4 Institute for Smart Infrastructure, Gangneung-Wonju National University, Gangneung 25457, Republic of Korea

1 Introduction

We consider the temporal evolution dynamics of phase-field models with Dirichlet boundary conditions on arbitrary shaped domains. The following phase-field models (1)–(3) are the Allen–Cahn (AC) [1–9], Cahn–Hilliard (CH) [9–13], nonlocal Cahn–Hilliard (nCH) [14, 15] equations, respectively:

$$\frac{\partial \psi}{\partial t} = -\frac{F'(\psi)}{\epsilon^2} + \Delta \psi, \tag{1}$$

$$\frac{\partial \psi}{\partial t} = \Delta \big[F'(\psi) - \epsilon^2 \Delta \psi \big], \tag{2}$$

$$\frac{\partial \psi}{\partial t} = \Delta \big[F'(\psi) - \epsilon^2 \Delta \psi \big] - \alpha(\psi - \bar{\psi}), \tag{3}$$

where $\psi = \psi(\mathbf{x}, t)$ is a phase-field, $\mathbf{x} \in \Omega$, and $t > 0$. We consider problems in two- and three-dimensional domains, $\Omega \subset \mathbb{R}^2$ or $\mathbb{R}^3$. Here, $F(\psi) = 0.25(\psi^2 - 1)^2$ (see Fig. 1), ϵ and α are positive constants, and $\bar{\psi} = \int_\Omega \psi(\mathbf{x}, 0)d\mathbf{x} \big/ \int_\Omega d\mathbf{x}$.
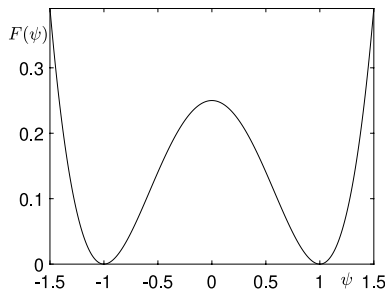
Fig. 1 Double-well potential free energy $F(\psi) = 0.25(\psi^2 - 1)^2$

The AC equation (1) is a mathematical equation that models the process of anti-phase domain coarsening in crystalline solids [2]. It can be derived from the L^2-gradient flow of the Ginzburg–Landau free-energy functional [16, 17]:

$$\mathcal{E}(\psi) = \int_\Omega \left(\frac{F(\psi)}{\epsilon^2} + \frac{1}{2}|\nabla\psi|^2 \right) d\mathbf{x}. \tag{4}$$
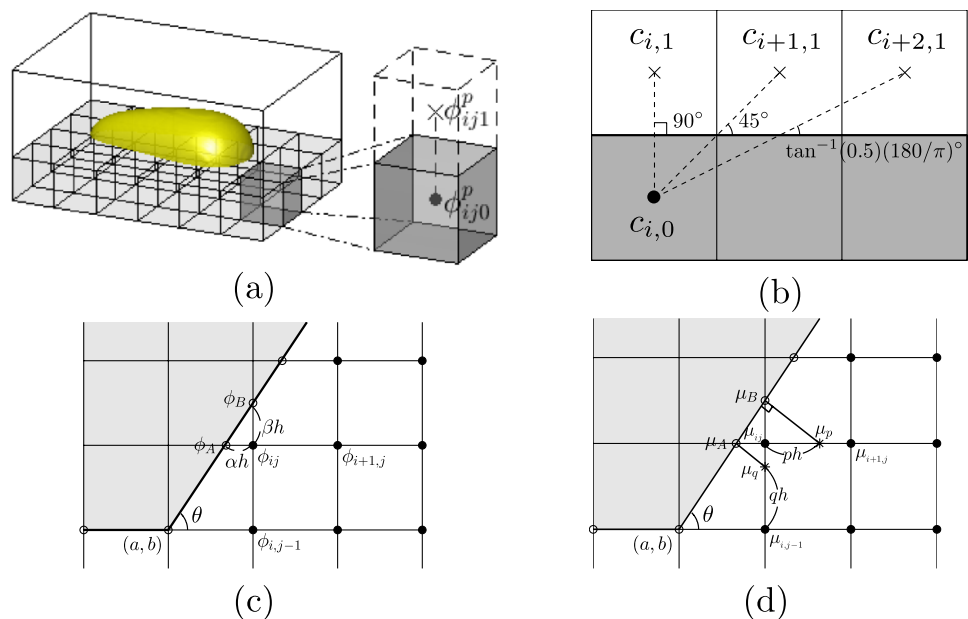
The AC equation satisfies the maximum principle, which means that if the initial condition is bounded by one, then the solution of the AC equation remains bounded by one for any time [18]. Furthermore, the energy functional (4) decreases with time, expressed as $d\mathcal{E}(\psi)/dt \le 0$ [18, 19]. The AC equation has been widely applied to various fields, including image segmentation [20], multiphase flow [21], crystal growth, volume repairing [22], motion by mean curvature [23], and volume inpainting [24]. Zhang et al. [25] developed a class of high-order maximum principle preserving schemes for solving the AC equation. Tan and

Zhang [26] performed an analysis for a novel second-order numerical method for the AC equation. Zhang et al. [27] proposed non-iterative and temporally second-order accurate numerical methods for the anisotropic conservative AC equation. Wang et al. [28] proposed a linear energy stable and maximum principle preserving scheme with a novel stabilization approach for the AC equation. The CH equation (2) is a mathematical equation that describes the process of phase separation [10]. It can be derived from a gradient flow in a Hilbert space of the Ginzburg–Landau free-energy functional (4).

There are various boundary conditions such as homogeneous Neumann [29–31], periodic [31–33], contact angle [34, 35], pinning [36], dynamic, crack, Robin-type [37], pseudo-Neumann [38, 39], reflecting [40], Dirichlet [41–43] boundary conditions for the phase-field models. Research on curvature-driven pattern formation on evolving domains has been conducted by adding phyllotaxis [44–46] to the CH-type phase-field model [47]. For example, the pinning boundary condition was used to simulate the coffee ring effect during the drying of a droplet [36], see Fig. 2(a) for a schematic illustration. Figure 2b shows the contact angle boundary condition [34]. Figure 2c, d display the Dirichlet and Neumann boundary conditions [48], respectively. For a more detailed explanation of the numerical treatments, please see the corresponding references.

The primary objective of the present study is to explore the temporal evolution dynamics of the phase-field models with Dirichlet boundary conditions on arbitrary shaped domains. The main finding is that we can effectively impose perpendicular boundary conditions by setting the zero Dirichlet boundary condition, which proves to be

Fig. 2 **a** Schematics of the pinning boundary condition in a 3D space, **b** the contact angle boundary condition, **c** the Dirichlet boundary condition, and **d** the Neumann boundary condition. Reprinted from [34, 36, 48] with permission from the publisher

(a)

(b)

(c)

(d)

highly useful and efficient in complex-shaped domains. Calculating perpendicular boundary conditions in domains with complex shapes is a challenging problem [48]. Methods such as interpolation and the use of indicator functions need to be considered; however, the method we propose is a simpler approach. This idea can be applied to other reaction-diffusion systems exhibiting Turing instability. Unstable critical values may be chosen as the Dirichlet boundary values to obtain effective perpendicular boundary conditions.

The outline of this paper is as follows. Section 2 describes the proposed numerical methodology. In Sect. 3, the computational experiments are conducted. Conclusions are provided in Sect. 4.

2 Numerical method

2.1 Two-dimensional numerical method

Let $\Omega = (L_x, R_x) \times (L_y, R_y)$ be the domain and let the discrete domain be $\Omega_h = \{(x_i = L_x + ih, \ y_j = L_y + jh) \mid i = 0, \ldots, N_x, \ j = 0, \ldots, N_y\}$ with $h = (R_x - L_x)/N_x$; see Fig. 3.

For simplicity of notation, let $\psi_{ij}^n = \psi(x_i, y_j, n\Delta t)$, where Δt is the time step. Since we use Dirichlet boundary condition, $\psi_{0j} = 0$, $\psi_{N_x j} = 0$, $\psi_{i0} = 0$, and $\psi_{iN_y} = 0$ for $i = 0, 1, \ldots, N_x$, and $j = 0, 1, \ldots, N_y$ when solving the AC equation. We note that $\psi = -1, 0, 1$ are critical points, among which $\psi = 0$ is an unconditionally unstable critical point [50]. The primary finding of this study is to set the unconditionally unstable point as the boundary value and obtain the perpendicular effect at the boundary when phases separate.

Using the fully explicit Euler method, the AC Eq. (1) is discretized as follows:

$$\frac{\psi_{ij}^{n+1} - \psi_{ij}^n}{\Delta t} = -\frac{\left(\psi_{ij}^n\right)^3 - \psi_{ij}^n}{\epsilon^2} + \Delta_d \psi_{ij}^n, \tag{5}$$

where $\Delta_d \psi_{ij} = (\psi_{i-1,j} + \psi_{i+1,j} - 4\psi_{ij} + \psi_{i,j-1} + \psi_{i,j+1})/h^2$. Equation (5) can be rewritten as

$$\psi_{ij}^{n+1} = \psi_{ij}^n + \Delta t \left(-\frac{\left(\psi_{ij}^n\right)^3 - \psi_{ij}^n}{\epsilon^2} + \Delta_d \psi_{ij}^n \right). \tag{6}$$

The CH Eq. (2) is discretized using the linear convex splitting-type scheme [51]:

$$\frac{\psi_{ij}^{n+1} - \psi_{ij}^n}{\Delta t} = \Delta_d \left[\left(\psi_{ij}^n\right)^3 - 3\psi_{ij}^n + 2\psi_{ij}^{n+1} \right] - \epsilon^2 \Delta_d^2 \psi_{ij}^{n+1} \tag{7}$$

$$= \Delta_d \left[\left(\psi_{ij}^n\right)^3 - 3\psi_{ij}^n \right] + 2\Delta_d \psi_{ij}^{n+1} - \epsilon^2 \Delta_d^2 \psi_{ij}^{n+1}, \tag{8}$$

where we have used the linear splitting of $\psi^3 - \psi = \psi^3 - 3\psi + 2\psi$ and

$$\begin{aligned}
\Delta_d^2 \psi_{ij} &= \Delta_d\left(\Delta_d \psi_{ij}\right) \\
&= \frac{\Delta_d \psi_{i-1,j} + \Delta_d \psi_{i+1,j} - 4\Delta_d \psi_{ij} + \Delta_d \psi_{i,j-1} + \Delta_d \psi_{i,j+1}}{h^2} \\
&= \left[\psi_{i-2,j} + \psi_{i+2,j} + \psi_{i,j-2} + \psi_{i,j+2} \right. \\
&\quad + 2(\psi_{i-1,j-1} + \psi_{i-1,j+1} + \psi_{i+1,j-1} \\
&\quad + \psi_{i+1,j+1}) - 8(\psi_{i-1,j} + \psi_{i+1,j} + \psi_{i,j-1} \\
&\quad \left. + \psi_{i,j+1}) + 20\psi_{ij}\right]/h^4.
\end{aligned}$$

Due to the use of the discrete biharmonic operator, an extended discrete domain is required, as illustrated in Fig. 4. When solving the CH and nCH equations, ghost points are needed: $\psi_{-1,j} = 0$, $\psi_{0,j} = 0$, $\psi_{N_x,j} = 0$, $\psi_{N_x+1,j} = 0$, $\psi_{i,-1} = 0$, $\psi_{i,0} = 0$, $\psi_{i,N_y} = 0$, and $\psi_{i,N_y+1} = 0$ for $i = 0, 1, \ldots, N_x$ and $j = 0, 1, \ldots, N_y$. The use of ghost points, as depicted in Fig. 4, effectively introduces a homogeneous Neumann boundary condition, which ensures that the interface is perpendicular to the boundary [52].

We use the following Saul'yev-type method [53] for Eq. (11), which is a better scheme than Fourier spectral method [54] on complex domains:
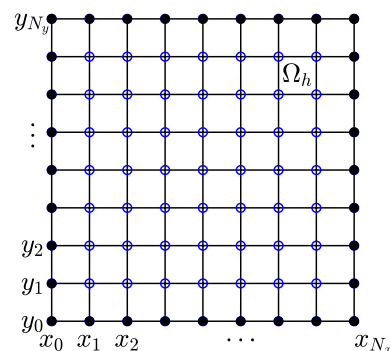

Fig. 3 Schematic illustrations of the discrete numerical domains Ω_h for the AC equation
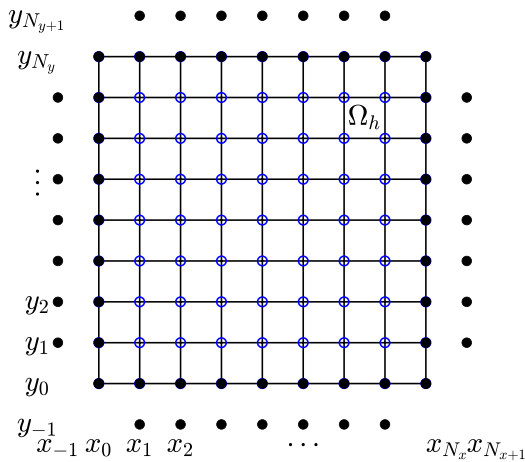
Fig. 4 Schematic illustrations of the discrete numerical domains Ω_h for the CH and nCH equations

For $j = 1, 2, \ldots, N_y - 1$, for $i = 1, 2, \ldots, N_x - 1$,

$$
\frac{\psi_{ij}^{n+1} - \psi_{ij}^n}{\Delta t} = \Delta_d \left[(\psi_{ij}^n)^3 - 3\psi_{ij}^n \right] + \frac{2}{h^2} \left(\psi_{i-1,j}^{n+1} + \psi_{i+1,j}^n \right.
$$
$$
- 2\psi_{ij}^n - 2\psi_{ij}^{n+1}
$$
$$
+ \psi_{i,j-1}^{n+1} + \psi_{i,j+1}^n \bigg) - \frac{\epsilon^2}{h^4} \left[\psi_{i-2,j}^{n+1} + \psi_{i+2,j}^n + \psi_{i,j-2}^{n+1} \right.
$$
$$
+ \psi_{i,j+2}^n + 2(\psi_{i-1,j-1}^{n+1} + \psi_{i-1,j+1}^n
$$
$$
+ \psi_{i+1,j-1}^{n+1} + \psi_{i+1,j+1}^n) - 8(\psi_{i-1,j}^{n+1} + \psi_{i+1,j}^n
$$
$$
+ \psi_{i,j-1}^{n+1} + \psi_{i,j+1}^n) + 10\psi_{ij}^n + 10\psi_{ij}^{n+1} \bigg]. \tag{9}
$$

We can simplify Eq. (9) as

$$
\psi_{ij}^{n+1} = \frac{1}{r} \left\{ \frac{\psi_{ij}^n}{\Delta t} + \Delta_d \left[(\psi_{ij}^n)^3 - 3\psi_{ij}^n \right] \right.
$$
$$
+ \frac{2}{h^2} \left(\psi_{i-1,j}^{n+1} + \psi_{i+1,j}^n - 2\psi_{ij}^n \right.
$$
$$
+ \psi_{i,j-1}^{n+1} + \psi_{i,j+1}^n \bigg) - \frac{\epsilon^2}{h^4} \left[\psi_{i-2,j}^{n+1} + \psi_{i+2,j}^n \right.
$$
$$
+ \psi_{i,j-2}^{n+1} + \psi_{i,j+2}^n + 2(\psi_{i-1,j-1}^{n+1} + \psi_{i-1,j+1}^n
$$
$$
+ \psi_{i+1,j-1}^{n+1} + \psi_{i+1,j+1}^n) - 8(\psi_{i-1,j}^{n+1} + \psi_{i+1,j}^n
$$
$$
\psi_{i,j-1}^{n+1} + \psi_{i,j+1}^n) + 10\psi_{ij}^n \big] \bigg\}, \tag{10}
$$

where $r = 1/\Delta t + 4/h^2 + 10\epsilon^2/h^4$. Figure 5 a visual explanation of the loop of Eq. (9). The ψ values of each node used to obtain ψ_{ij}^{n+1} are updated based on the loop.

The other 7 cases come into being as following:

For $j = 1, 2, \ldots, N_y - 1$, for $i = N_x - 1, N_x - 2, \ldots, 1$,

For $j = N_y - 1, N_y - 2, \ldots, 1$, for $i = 1, 2, \ldots, N_x - 1$,

For $j = N_y - 1, N_y - 2, \ldots, 1$, for $i = N_x - 1, N_x - 2, \ldots, 1$,

For $i = 1, 2, \ldots, N_x - 1$, for $j = 1, 2, \ldots, N_y - 1$,

For $i = N_x - 1, N_x - 2, \ldots, 1$, for $j = 1, 2, \ldots, N_y - 1$,

For $i = 1, 2, \ldots, N_x - 1$, for $j = N_y - 1, N_y - 2, \ldots, 1$,

For $i = N_x - 1, N_x - 2, \ldots, 1$, for $j = N_y - 1, N_y - 2, \ldots, 1$.

More details about the discretization of the CH equation can be found in the work of [53], which is an explicit version (alternating direction explicit, ADE) of an implicit formulation (alternating direction implicit, ADI) [55]. A conservative Saul'yev method for Eq. (2) is discussed in detail in [53]. As for the nCH Eq. (3), it is discretized using the linear convex splitting-type method [56]:

$$
\frac{\psi_{ij}^{n+1} - \psi_{ij}^n}{\Delta t} = \Delta_d \left[\left(\psi_{ij}^n \right)^3 - 3\psi_{ij}^n \right]
$$
$$
+ 2\Delta_d \psi_{ij}^{n+1} - \epsilon^2 \Delta_d^2 \psi_{ij}^{n+1} - \alpha \left(\psi_{ij}^{n+1} - \bar{\psi} \right). \tag{11}
$$

Next, we use the following Saul'yev-type method [57] for Eq. (11):

For $j = 1, 2, \ldots, N_y - 1$, for $i = 1, 2, \ldots, N_x - 1$,

$$
\frac{\psi_{ij}^{n+1} - \psi_{ij}^n}{\Delta t} = \Delta_d \left[\left(\psi_{ij}^n \right)^3 - 3\psi_{ij}^n \right]
$$
$$
+ \frac{2}{h^2} \left(\psi_{i-1,j}^{n+1} + \psi_{i+1,j}^n - 2\psi_{ij}^n - 2\psi_{ij}^{n+1} \right)
$$
$$
+ \psi_{i,j-1}^{n+1} + \psi_{i,j+1}^n - \frac{\epsilon^2}{h^4} \left[\psi_{i-2,j}^{n+1} + \psi_{i+2,j}^n \right.
$$
$$
+ \psi_{i,j-2}^{n+1} + \psi_{i,j+2}^n + 2\left(\psi_{i-1,j-1}^{n+1} + \psi_{i-1,j+1}^n \right)
$$
$$
+ \psi_{i+1,j-1}^{n+1} + \psi_{i+1,j+1}^n - 8(\psi_{i-1,j}^{n+1} + \psi_{i+1,j}^n + \psi_{i,j-1}^{n+1}
$$
$$
+ \psi_{i,j+1}^n) + 10\psi_{ij}^n + 10\psi_{ij}^{n+1} \big]
$$
$$
- \alpha(\psi_{ij}^{n+1} - \bar{\psi}). \tag{12}
$$

Equation (12) is rewritten as

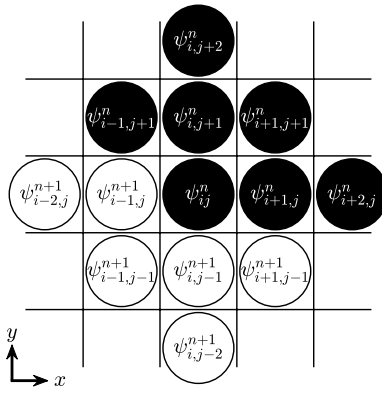**Fig. 5** Schematic visualization of the loop: For $j = 1, 2, \ldots, N_y - 1$, for $i = 1, 2, \ldots, N_x - 1$

$$
\psi_{ij}^{n+1} = \frac{1}{r} \left\{ \frac{\psi_{ij}^n}{\Delta t} + \Delta_d \left[(\psi_{ij}^n)^3 - 3\psi_{ij}^n \right] \right.
$$
$$
+ \frac{2}{h^2} \left(\psi_{i-1,j}^{n+1} + \psi_{i+1,j}^n - 2\psi_{ij}^n \right.
$$
$$
\left. + \psi_{i,j-1}^{n+1} + \psi_{i,j+1}^n \right) - \frac{\epsilon^2}{h^4} \left[\psi_{i-2,j}^{n+1} + \psi_{i+2,j}^n + \psi_{i,j-2}^{n+1} \right.
$$
$$
+ \psi_{i,j+2}^n + 2(\psi_{i-1,j-1}^{n+1} + \psi_{i-1,j+1}^n
$$
$$
+ \psi_{i+1,j-1}^{n+1} + \psi_{i+1,j+1}^n) - 8(\psi_{i-1,j}^{n+1} + \psi_{i+1,j}^n + \psi_{i,j-1}^{n+1}
$$
$$
\left. \left. + \psi_{i,j+1}^n) + 10\psi_{ij}^n \right] + \alpha\bar\psi \right\}. \tag{13}
$$

where $r = 1/\Delta t + 4/h^2 + 10\epsilon^2/h^4 + \alpha$. For the remaining seven cases, the loops are identical to those of the CH equation. For additional information about the discretization of the nCH equation using a conservative Saul'yev method, please refer to [57].

2.2 Three-dimensional numerical method

We consider three-dimensional (3D) numerical method for nCH equation. Let the domain be $\Omega = (L_x, R_x) \times (L_y, R_y) \times (L_z, R_z)$ and the discrete domain be $\Omega_h = \{(x_i = L_x + ih, y_j = L_y + jh, z_k = L_z + kh) | i = 0, 1, \ldots, N_x, j = 0, 1, \ldots, N_y, k = 0, 1, \ldots, N_z\}$, with uniform grid size $h = (R_x - L_x)/N_x = (R_y - L_y)/N_y = (R_z - L_z)/N_z$. The nCH Eq. (3) is discretized using the linear convex splitting-type method [56]:

$$
\frac{\psi_{ijk}^{n+1} - \psi_{ijk}^n}{\Delta t} = \Delta_d \left[(\psi_{ijk}^n)^3 - 3\psi_{ijk}^n \right]
$$
$$
+ 2\Delta_d \psi_{ijk}^{n+1} - \epsilon^2 \Delta_d^2 \psi_{ijk}^{n+1} - \alpha(\psi_{ijk}^{n+1} - \bar\psi). \tag{14}
$$

Next, we use the following Saul'yev-type method [57] for Eq. (14):

For $k = 1, 2, \ldots, N_z - 1$, for $j = 1, 2, \ldots, N_y - 1$, for $i = 1, 2, \ldots, N_x - 1$

$$
\frac{\psi_{ijk}^{n+1} - \psi_{ijk}^n}{\Delta t} = \Delta_d \left[(\psi_{ijk}^n)^3 - 3\psi_{ijk}^n \right]
$$
$$
+ \frac{2}{h^2} \left(\psi_{i-1,jk}^{n+1} + \psi_{i+1,jk}^n + \psi_{i,j-1,k}^{n+1} \right.
$$
$$
\left. + \psi_{i,j+1,k}^n + \psi_{ij,k-1}^{n+1} + \psi_{ij,k+1}^n - 3\psi_{ijk}^n - 3\psi_{ijk}^{n+1} \right)
$$
$$
- \frac{\epsilon^2}{h^4} \left[\psi_{i-2,jk}^{n+1} + \psi_{i+2,jk}^n \right.
$$
$$
+ \psi_{i,j-2,k}^{n+1} + \psi_{i,j+2,k}^n + \psi_{ij,k-2}^n
$$
$$
+ \psi_{ij,k+2}^n + 2(\psi_{i-1,j-1,k}^{n+1} + \psi_{i-1,j+1,k}^n
$$
$$
+ \psi_{i+1,j-1,k}^{n+1} + \psi_{i+1,j+1,k}^n + \psi_{i-1,j,k-1}^{n+1}
$$
$$
+ \psi_{i-1,j,k+1}^n + \psi_{i+1,j,k-1}^n + \psi_{i+1,j,k+1}^n
$$
$$
+ \psi_{i,j-1,k-1}^{n+1} + \psi_{i,j-1,k+1}^n + \psi_{i,j+1,k-1}^n
$$
$$
+ \psi_{i,j+1,k+1}^n) - 12(\psi_{i-1,jk}^{n+1} + \psi_{i+1,jk}^n
$$
$$
+ \psi_{i,j-1,k}^{n+1} + \psi_{i,j+1,k}^n + \psi_{ij,k-1}^{n+1} + \psi_{ij,k+1}^n)
$$
$$
\left. + 21\psi_{ijk}^n + 21\psi_{ijk}^{n+1} \right] - \alpha(\psi_{ijk}^{n+1} - \bar\psi). \tag{15}
$$

Equation (15) is rewritten as

$$
\psi_{ijk}^{n+1} = \frac{1}{r} \left\{ \frac{\psi_{ijk}^n}{\Delta t} + \Delta_d \left[(\psi_{ijk}^n)^3 - 3\psi_{ijk}^n \right] \right.
$$
$$
+ \frac{2}{h^2} \left(\psi_{i-1,jk}^{n+1} + \psi_{i+1,jk}^n \right.
$$
$$
\left. + \psi_{i,j-1,k}^{n+1} + \psi_{i,j+1,k}^n + \psi_{ij,k-1}^{n+1} + \psi_{ij,k+1}^n - 3\psi_{ijk}^n \right)
$$
$$
- \frac{\epsilon^2}{h^4} \left[\psi_{i-2,jk}^{n+1} + \psi_{i+2,jk}^n \right.
$$
$$
+ \psi_{i,j-2,k}^{n+1} + \psi_{i,j+2,k}^n + \psi_{ij,k-2}^{n+1} + \psi_{ij,k+2}^n
$$
$$
+ 2(\psi_{i-1,j-1,k}^{n+1} + \psi_{i-1,j+1,k}^n + \psi_{i+1,j-1,k}^{n+1}
$$
$$
+ \psi_{i+1,j+1,k}^n + \psi_{i-1,j,k-1}^{n+1} + \psi_{i-1,j,k+1}^n
$$
$$
+ \psi_{i+1,j,k-1}^n + \psi_{i+1,j,k+1}^n + \psi_{i,j-1,k-1}^{n+1}
$$
$$
+ \psi_{i,j-1,k+1}^n + \psi_{i,j+1,k-1}^n + \psi_{i,j+1,k+1}^n)
$$
$$
- 12(\psi_{i-1,jk}^{n+1} + \psi_{i+1,jk}^n + \psi_{i,j-1,k}^{n+1}
$$
$$
+ \psi_{i,j+1,k}^n + \psi_{ij,k-1}^{n+1} + \psi_{ij,k+1}^n)
$$
$$
\left. \left. + 10\psi_{ijk}^n \right] + \alpha\bar\psi \right\}, \tag{16}
$$

where $r = 1/\Delta t + 6/h^2 + 21\epsilon^2/h^4 + \alpha$. For the other 47 cases, the loops are identical to those of the CH equation. Refer [57] to find details about the discretization using a conservative Saul'yev method for the nCH equation.

3 Numerical experiments

We perform various computational tests in different computational domains to investigate the temporal evolution dynamics of the phase-field models with Dirichlet boundary conditions.

3.1 Pattern formations in a rectangular domain

First, we consider the temporal evolutions of the computational solutions of the phase-field models on a simple rectangular domain $\Omega = (0,1) \times (0,1)$. The discrete computational domain for the AC equation is $\Omega_h = \{(x_i, y_j) | x_i = hi, \ y_j = hj, \text{ for } i = 0, \ldots, N_x, \ j = 0, \ldots, N_y\}$, where $h = 0.01$ and $N_x = N_y = 100$. For the CH and nCH equations, $\Omega_h = \{(x_i, y_j) | x_i = hi, \ y_j = hj, \text{ for } i = -1, \ldots, N_x + 1, \ j = -1, \ldots, N_y + 1\}$ is used. We use the initial condition

$$\psi_{ij}^0 = 0.15 \ \text{rand}(x_i, y_j), \tag{17}$$

where $\text{rand}(x_i, y_j)$ is a uniformly distribution random number in interval $(-1, 1)$. The parameters are $\Delta t = 0.1 h^2$, $\epsilon = h$, $\bar{\psi} = 0$, and $\alpha = 1000$.

Figure 6a–c show the numerical simulation result for the AC equation at times $t = 10\Delta t$, $50\Delta t$, and $200\Delta t$, respectively. Here, the zero Dirichlet boundary condition is applied. We can observe the interface of the phases contacts perpendicularly the domain boundary except a couple

of grids. Figure 6d shows plots of $\psi_{0:N_x,j}^{200}$ at $j = 0, 1, 2$, and 7. At the domain boundary $j = 0$, the phase-field is zero as we prescribed. On grid cell inside the domain, the phase-field takes non-zero values because zero is not stable value. As the j-index progressively increases, the phase-field approaches plus one or minus one with transition layers. Consequently, the interface (zero-level set of the phase-field) effectively forms perpendicular to the domain boundary.

Figure 7a–c show the numerical simulation results for the CH equation with homogeneous Dirichlet boundary condition at times $t = 400\Delta t$, $1200\Delta t$, and $24,000\Delta t$, respectively. We can observe the interface of the phases contacts perpendicularly the domain boundary except a couple of grids and phase separation occurs inside domain. Figure 7d shows plots of $\psi_{0:N_x,j}^{24000}$ at $j = 0, 1, 2$, and 7. The profiles are similar to the case of the AC equation.

Figure 8a–c show the numerical simulation results for the nCH equation with zero Dirichlet boundary condition at times $t = 400\Delta t$, $1200\Delta t$, and $40000\Delta t$, respectively. We can observe the interface of the phases contacts perpendicularly the domain boundary except a couple of grids, phase separation occurs inside domain, and lamellar structures are formed. Figure 8d shows plots of $\psi_{0:N_x,j}^{40,000}$ at $j = 0, 1, 2$, and 7. The profiles are similar to the cases of the AC and CH equations except that the maximum and minimum values are limited by some value less than one and greater than minus one, respectively.

Fig. 6 Temporal evolution of the computational solutions of the AC equation: **a–c** are at times $t = 10\Delta t$, $50\Delta t$, and $200\Delta t$, respectively. **d** Plots of $\psi_{0:N_x,j}^{200}$ at $j = 0, 1, 2$, and 7
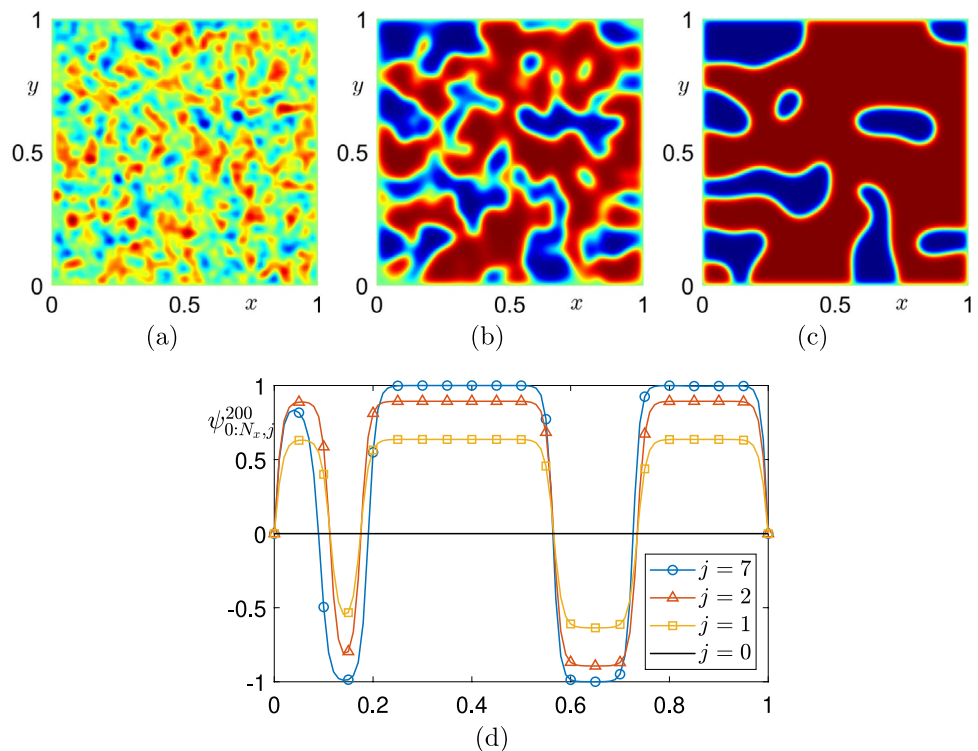
Fig. 7 Temporal evolution of the computational solutions of the CH equation: **a–c** are at times $t = 400\Delta t$, $1200\Delta t$, and $24000\Delta t$, respectively. (d) Plots of $\psi_{0:N_x,j}^{24000}$ at $j = 0, 1, 2$, and 7
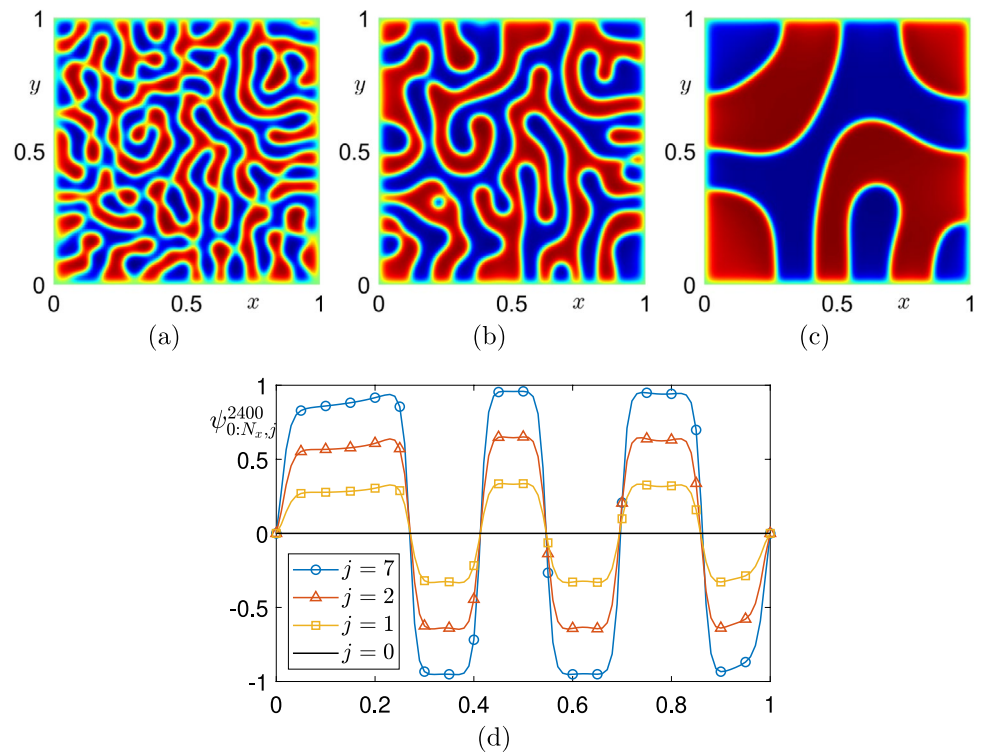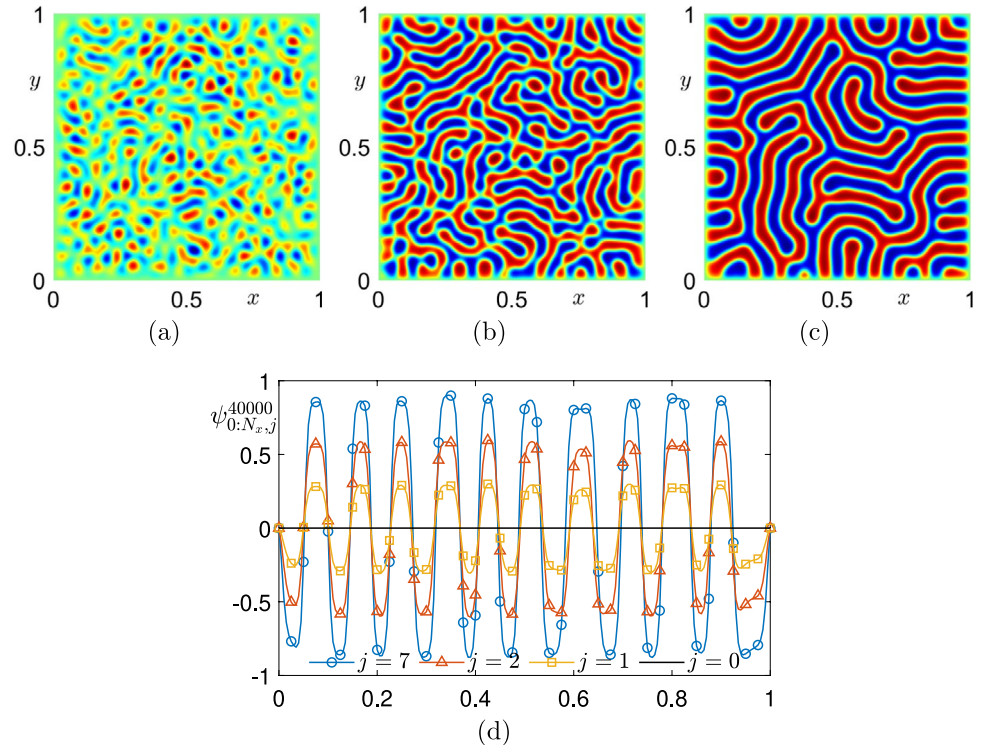

Fig. 8 Temporal evolution of the numerical solutions of the nCH equation: **a–c** are at $t = 400\Delta t$, $1200\Delta t$, and $40,000\Delta t$, respectively. **d** Plots of $\psi_{0:N_x,j}^{40000}$ at $j = 0, 1, 2$, and 7

3.2 Pattern formations in an elliptical domain

This subsection is concerned with pattern formations in an elliptical domain Ω which is embedded in $\Omega_e = (-10, 10) \times (-10, 10)$. Here, the parameters are $N_x = N_y = 500$, $h = 0.04$, $\Delta t = 0.1h^2$, $\epsilon = h$, $\bar{\psi} = 0$, and $\alpha = 100$. The discrete computational domain is given as

$$\Omega_h = \left\{ (x_i, y_j) \left| \left(\frac{2x_i}{9}\right)^2 + \left(\frac{2y_j}{11}\right)^2 < 1 \right. \right\}, \qquad (18)$$

where $x_i = -10 + hi$ for $i = 0, \ldots, N_x$ and $y_j = -10 + hj$ for $j = 0, \ldots, N_y$. We use the initial condition

$$\psi_{ij}^0 = 0.15 \ \mathrm{rand} \ (x_i, y_j), \ \text{for} \ (x_i, y_j) \in \Omega_h. \qquad (19)$$

Outside the domain, a zero Dirichlet boundary value is assigned, and we only update the values within the domain Ω_h.

Figure 9a–c display the temporal evolutions of the computational solutions of Eqs. (1)–(3), respectively. We can observe that the zero Dirichlet boundary condition effectively and efficiently achieves the perpendicular Neumann

boundary condition slightly away from the domain boundary. Implementing a conventional zero Neumann boundary condition in this case would be more complex.

3.3 Pattern formations in complex domains

Next, we present the results of computational experiments in more complex domains with Dirichlet boundary conditions. Let Ω be an arbitrary shaped open domain, and $\partial\Omega$ be its boundary of Ω, as shown in Fig. 10a. Additionally, let Ω_h be a discrete numerical domain, $\partial\Omega_h$ be its discrete boundary. For the AC equation, we use the discrete domain with a one-layer boundary, as illustrated in Fig. 10b. Because of the biharmonic term in the CH and

Fig. 9 Temporal evolutions of the computational solutions of **a** the AC, **b** CH, and **c** nCH equations. The times are shown below each figure
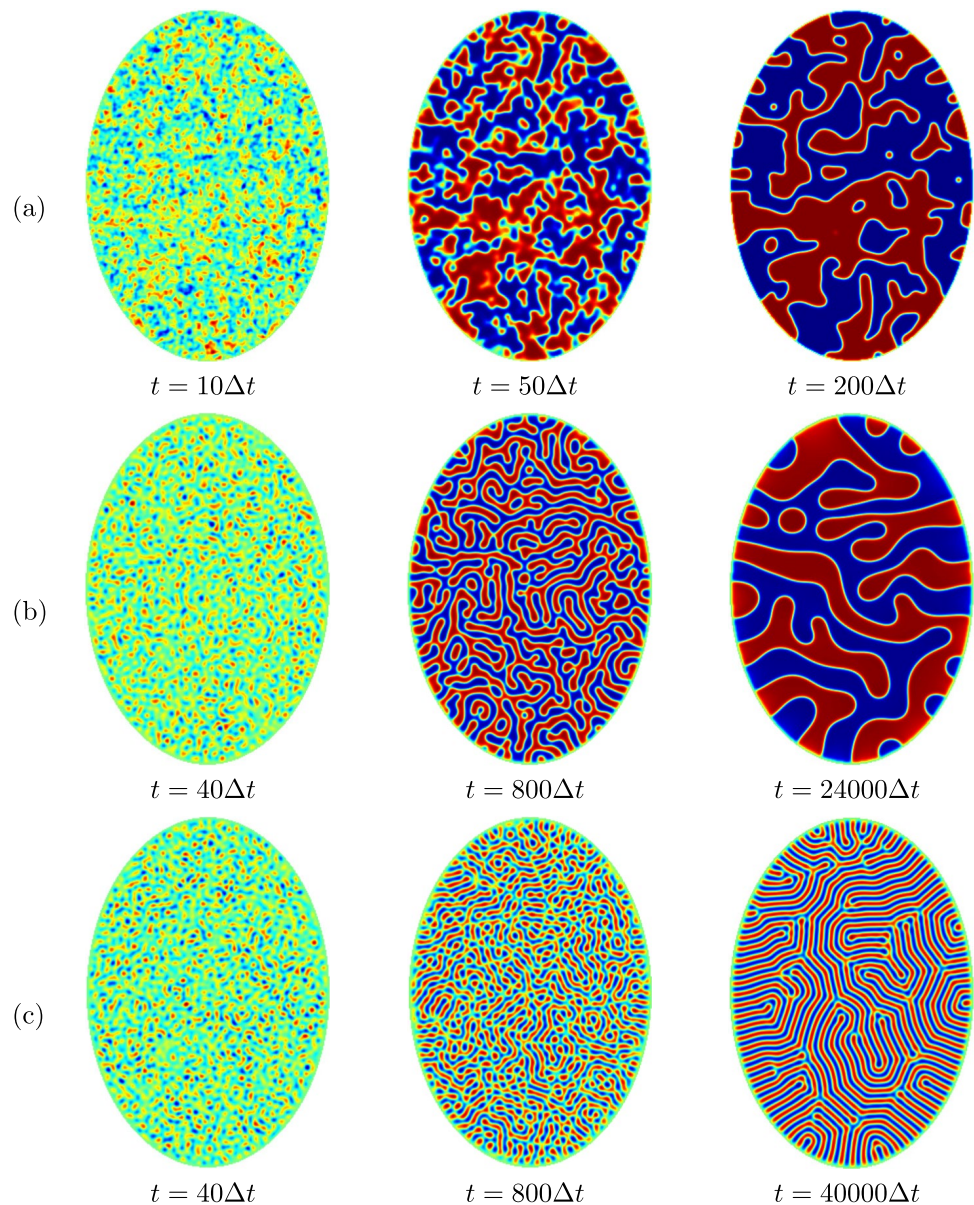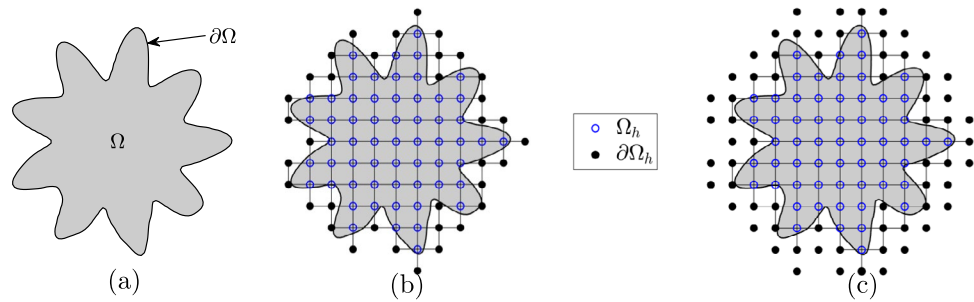

(a)

$t = 10\Delta t$ $t = 50\Delta t$ $t = 200\Delta t$

(b)

$t = 40\Delta t$ $t = 800\Delta t$ $t = 24000\Delta t$

(c)

$t = 40\Delta t$ $t = 800\Delta t$ $t = 40000\Delta t$

Fig. 10 **a** Complex domain Ω and its boundary $\partial\Omega$, **b** discrete complex domain Ω_h with one layer boundary for the AC equation and **c** discrete complex domain Ω_h with two layer boundaries for the CH and nCH equations

nCH equations, we use the discrete domain with two-layer boundaries, as depicted in Fig. 10c.

Let us consider an arbitrary shaped domain Ω embedded in $\Omega_e = (-10, 10) \times (-10, 10)$. Figure 11a–c display the numerical results of Eqs. (1)–(3) with zero Dirichlet boundary condition, respectively. The parameters specified are $N_x = N_y = 500$, $h = 0.04$, $\Delta t = 0.1h^2$, $\epsilon = h$, $\bar{\psi} = 0$, and $\alpha = 100$. The initial condition is

$$\psi_{ij}^0 = 0.15\,\mathrm{rand}(x_i, y_j), \quad \text{for } (x_i, y_j) \in \Omega_h. \tag{20}$$

We observe similar pattern formation results in the arbitrarily shaped domain when compared with the computational results in the rectangular domain.

Furthermore, we consider more complex domain with an elliptical hole inside, as shown in Fig. 12. We apply the homogeneous Dirichlet boundary condition in this case. The parameters specified are $N_x = N_y = 500$, $h = 0.04$,

Fig. 11 Temporal evolution results of the numerical solutions of **a** the AC equation, **b** the CH equation and **c** the nCH equation in complex domain
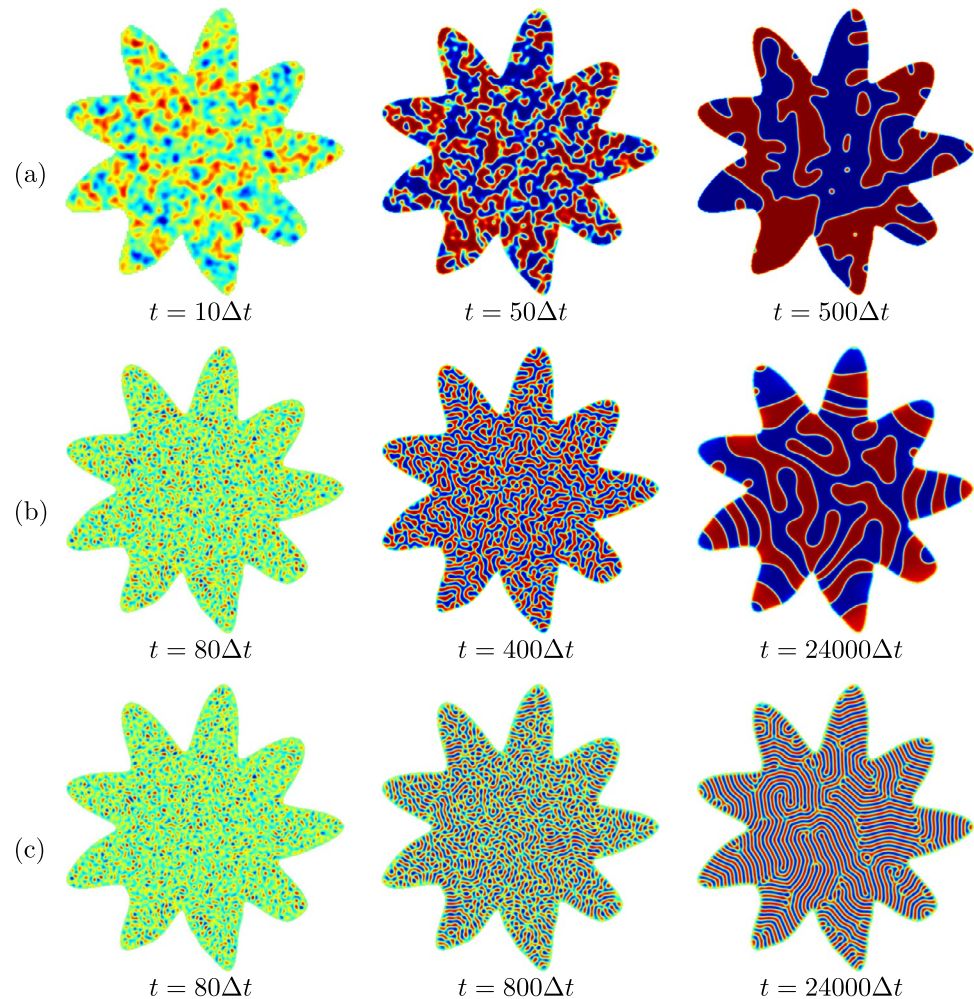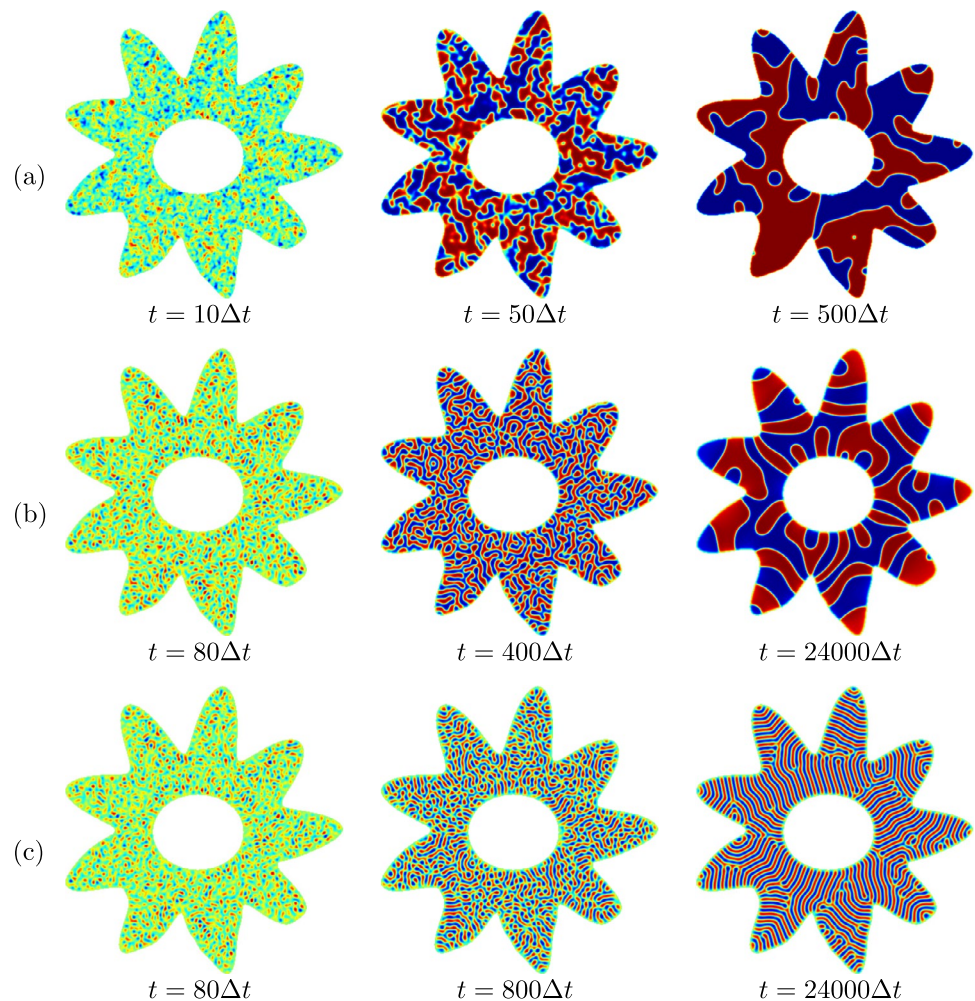

(a)

$t = 10\Delta t$ $t = 50\Delta t$ $t = 500\Delta t$

(b)

$t = 80\Delta t$ $t = 400\Delta t$ $t = 24000\Delta t$

(c)

$t = 80\Delta t$ $t = 800\Delta t$ $t = 24000\Delta t$

Fig. 12 Temporal evolution results of the numerical solutions of **a** the AC equation, **b** the CH equation, and **c** the nCH equation in more complex domain

(a)

$t = 10\Delta t$ $t = 50\Delta t$ $t = 500\Delta t$

(b)

$t = 80\Delta t$ $t = 400\Delta t$ $t = 24000\Delta t$

(c)

$t = 80\Delta t$ $t = 800\Delta t$ $t = 24000\Delta t$

$\Delta t = 0.1h^2$, $\epsilon = h$, $\bar{\psi} = 0$, and $\alpha = 100$. The initial condition is

$$\psi_{ij}^0 = 0.15 \, \text{rand}(x_i, y_j), \quad \text{for } (x_i, y_j) \in \Omega_h.$$

We can observe that all cases demonstrate the effective perpendicular Neumann boundary condition, even in the presence of a more complex domain with an elliptical hole.

Next, we explore the scenario where different non-zero Dirichlet boundary values are assigned inside and outside domain boundaries. Specifically, we set the boundary values as -1 inside the domain and 1 outside the domain. The computational results depicting the pattern formation are shown in Fig. 13. Figure 13a, b show that each boundary value dominates the corresponding phase region. Figure 13(c) shows that the pattern formation starts from the boundaries and results in alternating lamellar structures.

Numerical tests conducted in this study show a linear pattern for the nCH equation. Thus, we observe pattern formation in the nCH equation in more diverse domains. Set up the zebra-shaped domain and set the initial conditions to
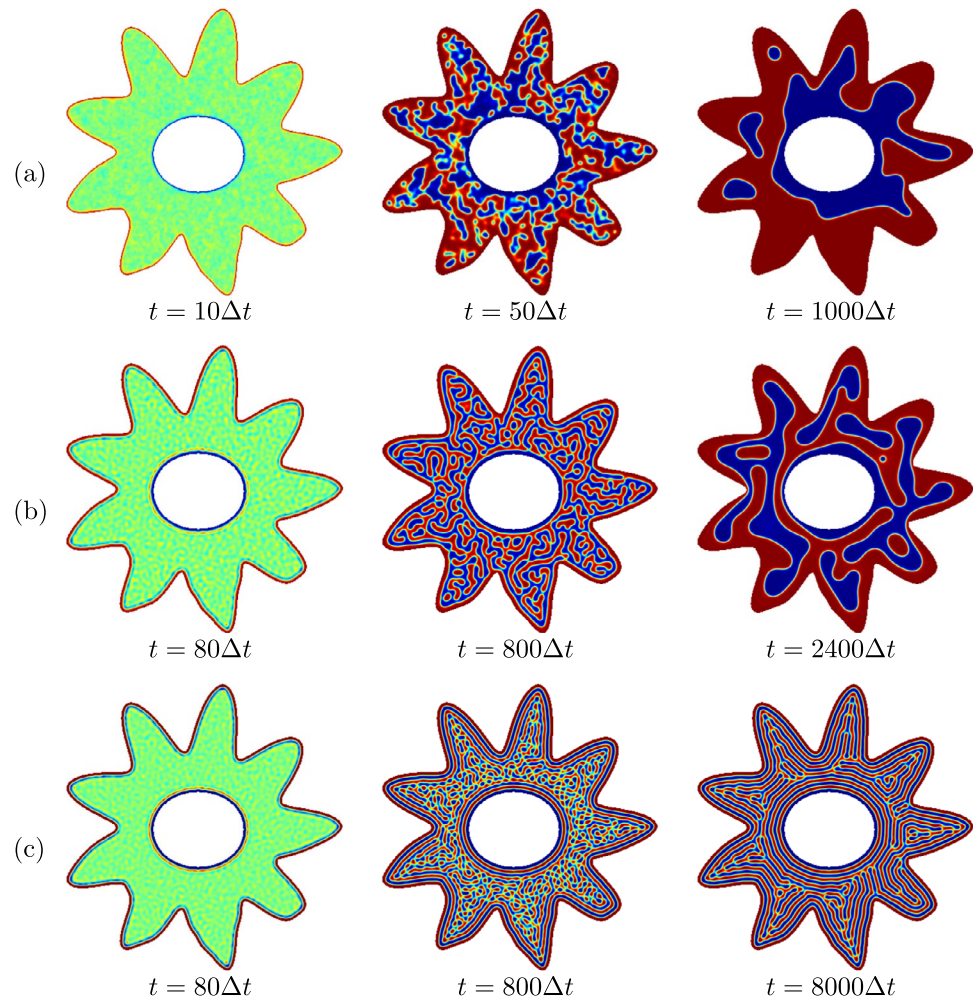
Eq. (20). The result is shown in Fig. 14. The zero Neumann boundary conditions are used and parameters are used as $N_x = 371$, $N_y = 331$, $h = 0.1$, $\Delta t = 0.1h^2$, $\epsilon = h$, $\bar{\psi} = 0$, and $\alpha = 10$. Figure 14c shows results similar to other tests conducted earlier in this paper.

3.4 Pattern formations with the 3D nCH equation

Finally, we consider three-dimensional numerical experiments to investigate pattern formation using the 3D nCH equation. First, the numerical test is proceeded in an ellipsoid domain. The domain is embedded in $\Omega_e = (-2, 2) \times (-2, 2) \times (-2, 2)$. We consider s computational domain

$$\Omega_h = \left\{ (x_i, y_j, z_k) \left| \tanh\left(\frac{1 - \sqrt{\frac{x_i^2}{3.61} + \frac{y_j^2}{1.96} + \frac{z_k^2}{1.96}}}{\sqrt{2}\epsilon} \right) > 0 \right. \right\},$$

(21)

Fig. 13 Temporal evolution results of the numerical solutions of **a** the AC equation, **b** the CH equation, and **c** the nCH equation with non-zero Dirichlet boundary condition in more complex domain

(a)

$t = 10\Delta t$ $t = 50\Delta t$ $t = 1000\Delta t$

(b)

$t = 80\Delta t$ $t = 800\Delta t$ $t = 2400\Delta t$

(c)

$t = 80\Delta t$ $t = 800\Delta t$ $t = 8000\Delta t$

for $i = 0, \ldots, N_x$, $j = 0, \ldots, N_y$, and $k = 0, \ldots, N_z$. We set the initial condition of $\psi(\mathbf{x}, 0)$ as random values between -0.15 and 0.15. The parameters specified are $N_x = N_y = N_z = 200$, $h = 0.02$, $\Delta t = h$, $\epsilon = h$, $\bar{\psi} = 0$, and $\alpha = 100$. Figure 15 shows pattern formation for the D nCH equation in an ellipsoid domain. We also observe results similar to the 2D results for the nCH equation.

Furthermore, we consider a more complex domain Ω that is embedded in $\Omega_e = (-1.5, 1.5) \times (-1.5, 1.5) \times (-1.5, 1.5)$. The parameters specified are $h = 0.02$, $\Delta t = h$, $\epsilon = h$, $\bar{\psi} = 0$, and $\alpha = 100$. Initial state of $\psi(\mathbf{x}, 0)$ is randomly assigned values between -0.15 and 0.15. In Fig. 16, the characteristic pattern formation of the nCH equation can be confirmed even in the complex domain. It can be seen that the nCH equation shows similar pattern formation for initial random values with Dirichlet boundary conditions.

3.5 Equilibrium states with various values of ϵ

We consider the equilibrium states for various values of ϵ. The AC equation is solved in a complex computational domain with a random initial condition $\psi_{ij}^0 = 0.5 + 0.5\text{rand}(x_i, y_j)$. In $\Omega_e = (-5, 5) \times (-5, 5)$, the parameters specified are $h = 0.04$, $\Delta t = 1.e\text{-}4$, and $tol = 1.e\text{-}7$. The error is defined as follows:

$$err_{ij}^n = \frac{\psi_{i+1,j}^n + \psi_{i-1,j}^n + \psi_{i,j+1}^n + \psi_{i,j-1}^n - 4\psi_{i,j}^n}{h^2}$$
$$- \frac{(\psi_{ij}^n)^3 - \psi_{ij}^n}{\epsilon^2}.$$

We assume that ψ^n is in an equilibrium state if $\|err^n\|_\infty < tol$ for some n.

Figure 17 shows the numerical solution of ψ in a complex computational domain for three different values of ϵ: $\sqrt{h}$, $\sqrt{10h}$, and $\sqrt{24h}$. Dai et al. [58] conducted a rigorous analysis of the equilibrium state that minimizes the energy functional based on the use of the Dirichlet boundary condition and the parameter ϵ, which represents the interface thickness. Similar dynamics of the equilibrium state with respect to ϵ values are observed in the results shown in Fig. 17.

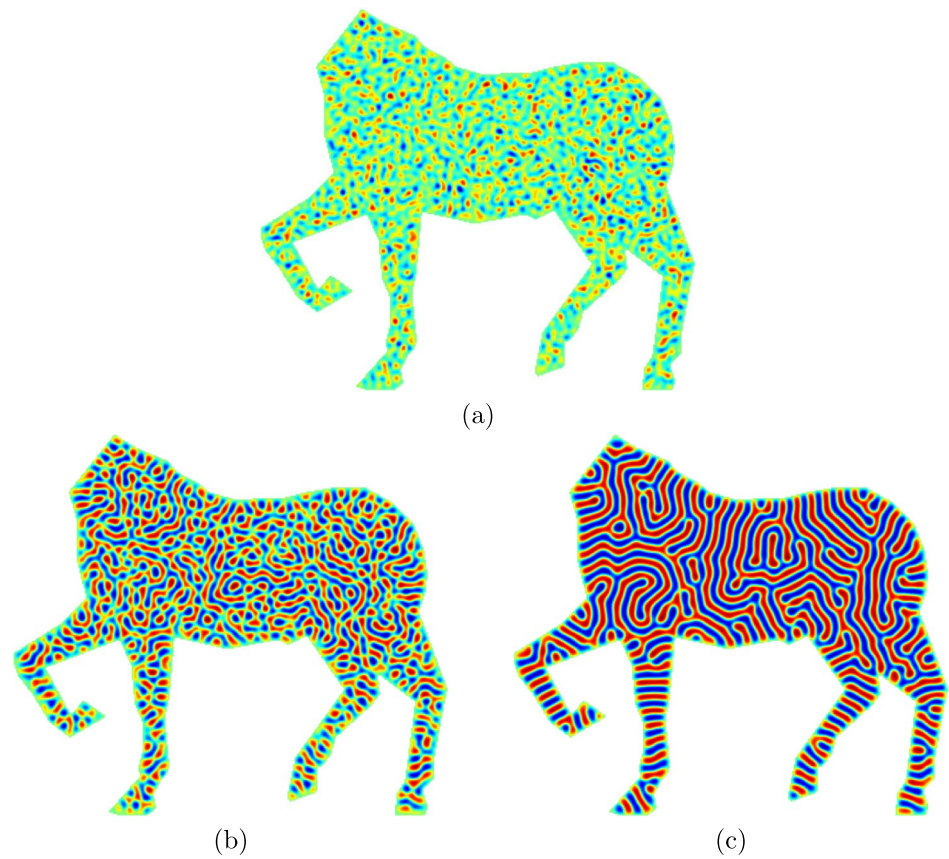**Fig. 14** Temporal evolution results when **a** $40\Delta t$, **b** $400\Delta t$, and **c** $4000\Delta t$

(a)

(b)　　　　(c)

Fig. 15 **a** is random initial statement. Temporal evolution results when **b** $t = 4.8$, and **c** $t = 622.08$
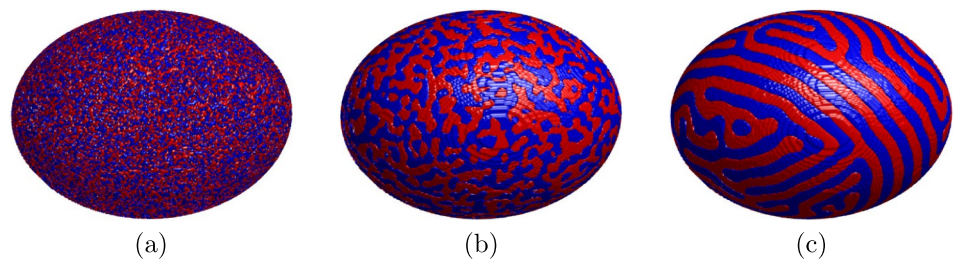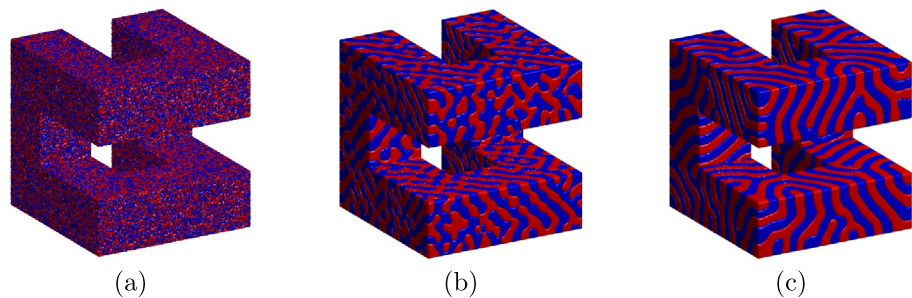

(a)　　　　(b)　　　　(c)

Fig. 16 **a** Random initial statement. Temporal evolution results when **b** $t = 24$, and **c** $t = 1152$

(a)　　　　(b)　　　　(c)

3.6 Non-rectangular mesh

In this section, we present a computational domain shaped like a dolphin as an example of triangulating a complex domain with an arbitrary geometry. The triangulated computational domain is illustrated in Fig. 18a. In the triangulated domain with N node points $\mathbf{x}_i = (x_i, y_i)$, the AC equation is discretized as follows:

Fig. 17 Equilibrium states in an arbitrary domain with **a** $\epsilon = \sqrt{h}$, **b** $\epsilon = \sqrt{10h}$, and **c** $\epsilon = \sqrt{24h}$
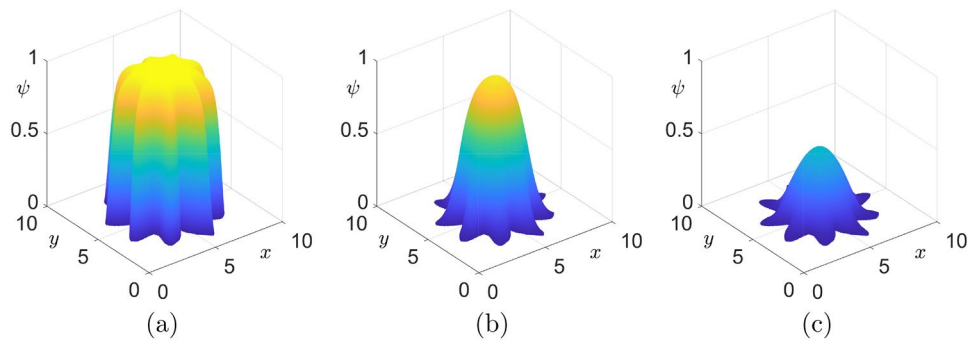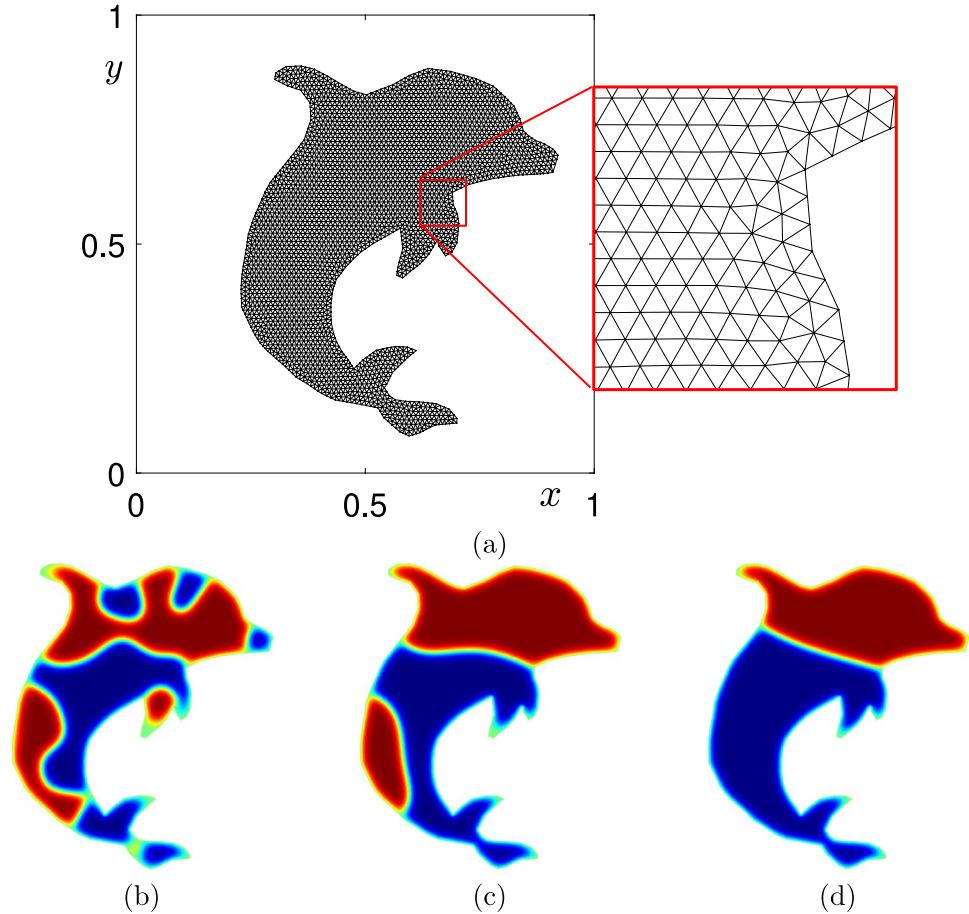

(a) (b) (c)

Fig. 18 **a** Triangulated computational domain in the shape of a dolphin. **b–d** Temporal evolution of the numerical solutions to the AC equation on a dolphin-shaped domain with randomly perturbed initial condition at $t = 100\Delta t$, $t = 520\Delta t$, and $t = 1760\Delta t$, respectively

(a)

(b) (c) (d)

$$\frac{\psi_i^{n+1} - \psi_i^n}{\Delta t} = -\frac{(\psi_i^n)^3 - \psi_i^n}{\epsilon^2} + \Delta_M \psi_i^n, \quad \text{for } 1 \leq i \leq N,$$

where $\psi_i^n = \psi(\mathbf{x}_i, n\Delta t)$ and Δ_M is the discrete Laplace operator [59], which is defined as

$$\Delta_M \psi_i = \frac{3}{A(\mathbf{x}_i)} \sum_{m=1}^{N_i} \frac{\cot \alpha_{i_m} + \cot \beta_{i_m}}{2} (\psi_{i_m} - \psi_i).$$

Here, $\mathbf{x}_m$ for $1 \leq m \leq N_i$ are 1-ring neighbor vertices of vertex $\mathbf{x}_i$, α_{i_m} and β_{i_m} are the angles formed by $\mathbf{x}_i$, $\mathbf{x}_m$, and the vertices adjacent to $\mathbf{x}_m$, respectively and $A(\mathbf{x}_i)$ is the sum of areas of triangles surrounding vertex $\mathbf{x}_i$. Figures 18b–d show the temporal evolution of the numerical solutions to the AC equation on a dolphin-shaped domain with randomly perturbed initial condition $\psi(\mathbf{x}, 0) = \text{rand}(\mathbf{x})$ at $t = 100\Delta t$, $t = 520\Delta t$, and $t = 1760\Delta t$, where $\text{rand}(\mathbf{x})$ is random value between -0.1 and 0.1. Here, we use 3058 nodes points, $\Delta t = 1e\text{-}5$, and $\epsilon = 0.01$.

4 Conclusions

In this paper, we have investigated both 2D and 3D temporal and spatial evolution dynamics of the phase-field models such as the AC, CH, and nCH equations with the Dirichlet boundary conditions on arbitrary shaped domains. Using different Dirichlet boundary conditions, we could successfully control the phase transformation dynamics of the phase-field models. For the nCH, labyrinth-type pattern formations were implemented through numerical simulations. We could effectively impose perpendicular boundary conditions by setting the zero Dirichlet boundary condition, which proven to be highly useful and efficient, especially in the complex-shaped domains. Consequently, our findings shed new light on the effective utilization of the zero Dirichlet boundary condition, demonstrating its superior utility and efficiency compared to alternative approaches. The successful imposition of perpendicular boundary conditions using the method opens up new possibilities for the exploration and analysis of phase-field models in complex-shaped domains.

Data availability The data that support the findings of this study are available from the corresponding author upon reasonable request.

Declarations

Conflict of interest The authors declare no Conflict of interest.

References

1. Hwang Y, Ham S, Lee C, Lee G, Kang S, Kim J (2023) A simple and efficient numerical method for the Allen-Cahn equation on effective symmetric triangular meshes. Electron Res Arch 31(8):4557–4578. https://doi.org/10.3934/era.2023233
2. Allen SM, Cahn JW (1979) A microscopic theory for antiphase boundary motion and its application to antiphase domain coarsening. Acta Metall 27(6):1085–1095. https://doi.org/10.1016/0001-6160(79)90196-2
3. Yang J, Chen J, Tan Z (2022) Highly efficient variant of SAV approach for two-phase incompressible conservative Allen-Cahn fluids. Eng Comput 38(6):5339–5357. https://doi.org/10.1007/s00366-022-01618-5
4. Feng J, Zhou Y, Hou T (2021) A maximum-principle preserving and unconditionally energy-stable linear second-order finite difference scheme for Allen-Cahn equations. Appl Math Lett 118:107179. https://doi.org/10.1016/j.aml.2021.107179
5. Cheng H, Yuan R (2022) The stability of traveling waves for Allen-Cahn equations with fractional Laplacian. Appl Anal 101(1):263–273. https://doi.org/10.1080/00036811.2020.1738399
6. Lee C, Choi Y, Kim J (2022) An explicit stable finite difference method for the Allen-Cahn equation. Appl Numer Math 182:87–99. https://doi.org/10.1016/j.apnum.2022.08.006
7. Rath B, Mao X, Jaiman RK (2023) An interface preserving and residual-based adaptivity for phase-field modeling of fully Eulerian fluid-structure interaction. J Comput Phys 488:112188. https://doi.org/10.1016/j.jcp.2023.112188
8. Lee D (2023) Computing the area-minimizing surface by the Allen-Cahn equation with the fixed boundary. AIMS Math 8(10):23352–23371. https://doi.org/10.3934/math.20231187
9. Fu Z, Yang J (2022) Energy-decreasing exponential time differencing Runge-Kutta methods for phase-field models. J Comput Phys 454:110943. https://doi.org/10.1016/j.jcp.2022.110943
10. Cahn JW (1961) On spinodal decomposition. Acta Metall 9:795–801. https://doi.org/10.1016/0001-6160(61)90182-1
11. Ren H, Zhuang X, Trung NT, Rabczuk T (2021) Nonlocal operator method for the Cahn-Hilliard phase field model. Commun Nonlinear Sci Numer Simul 96:105687. https://doi.org/10.1016/j.cnsns.2020.105687
12. Liao M, Wang D, Zhang C, Jia H (2023) The error analysis for the Cahn-Hilliard phase field model of two-phase incompressible flows with variable density. AIMS Math 8(12):31158–31185. https://doi.org/10.3934/math.20231595
13. Srinivasan A, Moure A, Gomez H (2024) Computational modeling of flow-mediated angiogenesis: Stokes-Darcy flow on a growing vessel network. Eng Comput 40(2):741–759. https://doi.org/10.1007/s00366-023-01889-6
14. Liu Z, Li X (2021) The fast scalar auxiliary variable approach with unconditional energy stability for nonlocal Cahn-Hilliard equation. Numer Methods Part Differ Equ 37(1):244–261. https://doi.org/10.1002/num.22527
15. Lee C, Kim S, Kwak S, Hwang Y, Ham S, Kang S, Kim J (2023) Semi-automatic fingerprint image restoration algorithm using a partial differential equation. AIMS Math 8(11):27528–27541. https://doi.org/10.3934/math.20231408
16. Bulaevskii LN, Ginzburg VL (1964) Temperature dependence of the shape of the domain wall in ferromagnetics and ferroelectrics. Sov Phys JETP 18(530):5
17. Lee D (2020) The numerical solutions for the energy-dissipative and mass-conservative Allen-Cahn equation. Comput Math Appl 80(1):263–284. https://doi.org/10.1016/j.camwa.2020.04.007
18. Hou T, Leng H (2020) Numerical analysis of a stabilized Crank-Nicolson/Adams-Bashforth finite difference scheme for Allen-Cahn equations. Appl Math Lett 102:106150. https://doi.org/10.1016/j.aml.2019.106150
19. Poochinapan K, Wongsaijai B (2022) Numerical analysis for solving Allen-Cahn equation in 1D and 2D based on higher-order compact structure-preserving difference scheme. Appl Math Comput 434:127374. https://doi.org/10.1016/j.amc.2022.127374
20. Lee D, Lee S (2019) Image segmentation based on modified fractional Allen-Cahn equation. Math Probl Eng. https://doi.org/10.1155/2019/3980181
21. Huang Z, Lin G, Ardekani AM (2022) Implementing contact angle boundary conditions for second-order phase-field models of wall-bounded multiphase flows. J Comput Phys 471:111619. https://doi.org/10.1016/j.jcp.2022.111619
22. Li Y, Lan S, Liu X, Lu B, Wang L (2020) An efficient volume repairing method by using a modified Allen-Cahn equation. Pattern Recognit 107:107478. https://doi.org/10.1016/j.patcog.2020.107478
23. Hwang Y, Kim I, Kwak S, Ham S, Kim S, Kim J (2023) Unconditionally stable monte carlo simulation for solving the

multi-dimensional Allen-Cahn equation. Electron Res Arch 31(8):5104–5123. https://doi.org/10.3934/era.2023261

24. Long J, Luo C, Yu Q, Li Y (2019) An unconditional stable compact fourth-order finite difference scheme for three dimensional Allen-Cahn equation. Comput Math Appl 77(4):1042–1054. https://doi.org/10.1016/j.camwa.2018.10.028

25. Zhang H, Yan J, Qian X, Song S (2021) Numerical analysis and applications of explicit high order maximum principle preserving integrating factor Runge-Kutta schemes for Allen-Cahn equation. Appl Numer Math 161:372–390. https://doi.org/10.1016/j.apnum.2020.11.022

26. Tan Z, Zhang C (2021) The discrete maximum principle and energy stability of a new second-order difference scheme for Allen-Cahn equations. Appl Numer Math 166:227–237. https://doi.org/10.1016/j.apnum.2021.04.010

27. Zhang J, Chen C, Yang X, Chu Y, Xia Z (2020) Efficient, non-iterative, and second-order accurate numerical algorithms for the anisotropic Allen-Cahn Equation with precise nonlocal mass conservation. J Comput Appl Math 363:444–463. https://doi.org/10.1016/j.cam.2019.05.003

28. Wang X, Kou J, Gao H (2021) Linear energy stable and maximum principle preserving semi-implicit scheme for Allen-Cahn equation with double well potential. Commun Nonlinear Sci Numer Simul 98:105766. https://doi.org/10.1016/j.cnsns.2021.105766

29. Dai D, Lv X, Wang Y (2020) Numerical simulation for a class of predator-prey system with homogeneous Neumann boundary condition based on a sinc function interpolation method. Bound Value Probl 2020:1–11. https://doi.org/10.1186/s13661-020-01402-8

30. Hu Y, Zhang S, He Q, Li D (2023) Diffuse interface-lattice Boltzmann modeling for heat and mass transfer with Neumann boundary condition in complex and evolving geometries. Int J Heat Mass Transf 215:124480. https://doi.org/10.1016/j.ijheatmasstransfer.2023.124480

31. Zhang A, Guo Z, Jiang B, Song J, Pan F, Xiong S (2022) Effect of laser shock on lamellar eutectic growth: A phase-field study. Int J Heat Mass Transf 183:122069. https://doi.org/10.1016/j.ijheatmasstransfer.2021.122069

32. Lee S, Shin J (2019) Energy stable compact scheme for Cahn-Hilliard equation with periodic boundary condition. Comput Math Appl 77(1):189–198. https://doi.org/10.1016/j.camwa.2018.09.021

33. Lee S, Lee D (2019) The fractional Allen-Cahn equation with the Sextic potential. Appl Math Comput 351:176–192. https://doi.org/10.1016/j.amc.2019.01.037

34. Lee HG, Kim J (2011) Accurate contact angle boundary conditions for the Cahn-Hilliard equations. Comput Fluids 44(1):178–186. https://doi.org/10.1016/j.compfluid.2010.12.031

35. Xia L, Chen F, Liu T, Du Zhang Y, Tian Dawei Zhang (2023) Phase-field simulations of droplet impact on superhydrophobic surfaces. Int J Mech Sci 240:107957. https://doi.org/10.1016/j.ijmecsci.2022.107957

36. Lee HG, Yang J, Kim J (2020) Pinning boundary conditions for phase-field models. Commun Nonlinear Sci Numer Simul 82:105060. https://doi.org/10.1016/j.cnsns.2019.105060

37. Knopf P, Lam KF (2020) Convergence of a Robin boundary approximation for a Cahn-Hilliard system with dynamic boundary conditions. Nonlinearity 33(8):4191. https://doi.org/10.1088/1361-6544/ab8351

38. Yang J, Wang J, Tan Z (2022) A simple and practical finite difference method for the phase-field crystal model with a strong nonlinear vacancy potential on 3D surfaces. Comput Math Appl 121:131–144. https://doi.org/10.1016/j.camwa.2022.07.012

39. Yang J, Tan Z (2022) Simple and practical method for the simulations of two-component PFC models for binary colloidal crystals

40. on curved surfaces. Int J Mech Sci 225:107342. https://doi.org/10.1016/j.ijmecsci.2022.107342

41. Jesus C, Sousa E (2021) Superdiffusion in the presence of a reflecting boundary. Appl Math Lett 112:106742. https://doi.org/10.1016/j.aml.2020.106742

42. Li Y, Jeong D, Shin J, Kim J (2013) A conservative numerical method for the Cahn-Hilliard equation with Dirichlet boundary conditions in complex domains. Comput Math Appl 65:102–115. https://doi.org/10.1016/j.camwa.2012.08.018

43. Barua AK, Chew R, Li S, Lowengub J, Münch A, Wagner B (2023) Sharp-interface problem of the Ohta-Kawasaki model for symmetric Diblock copolymers. J Comput Phys 481:112032. https://doi.org/10.1016/j.jcp.2023.112032

44. Kentheswaran K, Dietrich N, Tanguy S, Lalanne B (2022) Direct numerical simulation of gas-liquid mass transfer around a spherical contaminated bubble in the stagnant-cap regime. Int J Heat Mass Transf 198:123325. https://doi.org/10.1016/j.ijheatmasstransfer.2022.123325

45. Thompson DW (1917) On growth and form. Cambridge Univ, Press

46. Rivier N, Occelli R, Pantaloni J, Lissowski A (1984) Structure of Bénard convection cells, phyllotaxis and crystallography in cylindrical symmetry. Journal de physique 45(1):49–63

47. Rivier N, Sadoc JF, Charvolin J (2016) Phyllotaxis: a framework for foam topological evolution. Eur Phys J E 39:1–11. https://doi.org/10.1140/epje/i2016-16007-8

48. Rueda-Contreras MD, Romero-Arias JR, Aragon JL, Barrio RA (2018) Curvature-driven spatial patterns in growing 3D domains: a mechanochemical model for phyllotaxis. PLoS One 13(8):e0201746. https://doi.org/10.1371/journal.pone.0201746

49. Jeong D, Choi Y, Kim J (2016) Numerical investigation of local defectiveness control of diblock copolymer patterns. Condens Matter Phys 19(3):33001–33001. https://doi.org/10.5488/CMP.19.33001

50. Fang J, Wu C, Li J, Liu Q, Wu C, Sun G, Li Q (2019) Phase field fracture in elasto-plastic solids: Variational formulation for multi-surface plasticity and effects of plastic yield surfaces and hardening. Int J Mech Sci 156:382–396. https://doi.org/10.1016/j.ijmecsci.2019.03.012

51. Ham S, Jeong D, Kim H, Lee C, Kwak S, Hwang Y, Kim J (2022) Linear stability analysis of the Cahn-Hilliard equation in spinodal region. J Funct Space 2022(1):2970876. https://doi.org/10.1155/2022/2970876

52. Ham S, Li Y, Jeong D, Lee C, Kwak S, Hwang Y, Kim J (2022) An explicit adaptive finite difference method for the Cahn-Hilliard equation. J Nonlinear Sci 32(6):1–19. https://doi.org/10.1007/s00332-022-09844-3

53. Dai S, Luong T (2023) On the Cahn-Hilliard equation with no-flux and strong anchoring conditions. NoDea-Nonlinear Differ Equ Appl 30(4):49. https://doi.org/10.1007/s00030-023-00854-y

54. Yang J, Li Y, Lee C et al (2022) An explicit conservative Saul'yev scheme for the Cahn-Hilliard equation. Int J Mech Sci 217:106985. https://doi.org/10.1016/j.ijmecsci.2021.106985

55. Kim J, Kwak S, Lee HG, Hwang Y, Ham S (2023) A maximum principle of the Fourier spectral method for diffusion equations. Electron Res Arch 31(9):5396–5405. https://doi.org/10.3934/era.2023273

56. Kwak S, Kang S, Ham S, Hwang Y, Lee G, Kim J (2023) An unconditionally stable difference scheme for the two-dimensional modified Fisher-Kolmogorov-Petrovsky-Piscounov equation. J Math 2023(1):5527728. https://doi.org/10.1155/2023/5527728

57. Li Y, Xia Q, Lee C, Kim S, Kim J (2022) A robust and efficient fingerprint image restoration method based on a phase-field model. Pattern Recognit 123:108405. https://doi.org/10.1016/j.patcog.2021.108405

57. Yang J, Lee C, Jeong D, Kim J (2022) A simple and explicit numerical method for the phase-field model for diblock copolymer melts. Comput Mater Sci 205:111192. https://doi.org/10.1016/j.commatsci.2022.111192

58. Dai S, Li B, Luong T (2020) Minimizers for the Cahn-Hilliard energy functional under strong anchoring conditions. SIAM J Appl Math 80(5):2299–2317. https://doi.org/10.1137/19M1309651

59. Xu G (2004) Convergence of discrete Laplace-Beltrami operators over surfaces. Comput Math Appl 48(3–4):347–360. https://doi.org/10.1016/j.camwa.2004.05.001